

## RESEARCH ARTICLE

# CLUH couples mitochondrial distribution to the energetic and metabolic status

Jamal Wakim<sup>1</sup>, David Goudenege<sup>1</sup>, Rodolphe Perrot<sup>2</sup>, Naig Gueguen<sup>1</sup>, Valerie Desquirit-Dumas<sup>1</sup>, Juan Manuel Chao de la Barca<sup>1</sup>, Ilaria Dalla Rosa<sup>3</sup>, Florence Manero<sup>2</sup>, Morgane Le Mao<sup>1</sup>, Stephanie Chupin<sup>1</sup>, Arnaud Chevrollier<sup>1</sup>, Vincent Procaccio<sup>1</sup>, Dominique Bonneau<sup>1</sup>, David C. Logan<sup>4</sup>, Pascal Reynier<sup>1</sup>, Guy Lenaers<sup>1,‡</sup> and Salim Khiati<sup>1,‡</sup>

## ABSTRACT

Mitochondrial dynamics and distribution are critical for supplying ATP in response to energy demand. CLUH is a protein involved in mitochondrial distribution whose dysfunction leads to mitochondrial clustering, the metabolic consequences of which remain unknown. To gain insight into the role of CLUH on mitochondrial energy production and cellular metabolism, we have generated CLUH-knockout cells using CRISPR/Cas9. Mitochondrial clustering was associated with a smaller cell size and with decreased abundance of respiratory complexes, resulting in oxidative phosphorylation (OXPHOS) defects. This energetic impairment was found to be due to the alteration of mitochondrial translation and to a metabolic shift towards glucose dependency. Metabolomic profiling by mass spectroscopy revealed an increase in the concentration of some amino acids, indicating a dysfunctional Krebs cycle, and increased palmitoylcarnitine concentration, indicating an alteration of fatty acid oxidation, and a dramatic decrease in the concentrations of phosphatidylcholine and sphingomyeline, consistent with the decreased cell size. Taken together, our study establishes a clear function for CLUH in coupling mitochondrial distribution to the control of cell energetic and metabolic status.

**KEY WORDS:** CLUH, Metabolism, Mitochondria, Mitochondrial dynamics, Cell size

## INTRODUCTION

Mitochondrial morphology and ultrastructural organization are known to vary depending on the tissue and the physiological states considered (Benard et al., 2006), and many studies indicate that physical rearrangements, which involve remodeling of the inner membrane to modulate the form of the cristae, and changes of the balance between mitochondrial fission and fusion, affect mitochondrial energy production (Benard and Rossignol, 2008; Zick et al., 2009). In addition, mitochondrial motility and location within the cell are crucial for the maintenance of cell homeostasis and specific functions. For instance, mitochondria in spermatozooids are specifically located at the most proximal part of the flagellum to

supply ATP for sperm movement, while during apoptosis, active mitochondria aggregate near the nucleus, as an upstream event prior to cytochrome *c* release (Haga et al., 2003). Similar movements towards the nucleus have been observed during the process of mitophagy, where ubiquitylated mitochondria recruit p62 (also known as SQSTM1) and HDAC6 to promote their subsequent clearance (Lee et al., 2010). Further defects in mitochondrial transport and distribution have been found in neurons from a *Miro1* (also known as *Rhot1*)-deficient mouse, although mitochondrial respiration was normal (Nguyen et al., 2014). These examples demonstrate that both active and damaged mitochondria are subject to intense movements, which eventually could parallel metabolic modifications.

The CLU protein [known as CLUH (clustered mitochondria homolog) in mammals] was first identified in the slime mould *Dictyostelium discoideum* as a factor required for the proper distribution of mitochondria within the cytoplasm (Zhu et al., 1997). So far, CLU deficiency induces mitochondrial clustering in all organisms tested, including the protist *Dictyostelium discoideum* (Fields et al., 2002; Zhu et al., 1997), the yeast *Saccharomyces cerevisiae* (Fields et al., 1998), the plant *Arabidopsis thaliana* (El Zawily et al., 2014; Logan et al., 2003) and the animal *Drosophila melanogaster* (Cox and Spradling, 2009), as well as mouse embryonic fibroblasts (Gao et al., 2014) and human cancer cells (Gao et al., 2014). While CLU function is clearly required to prevent mitochondrial clustering, the mechanism responsible remains elusive. Fields et al. reported that in *cluA<sup>-</sup> Dictyostelium* cells, mitochondria were connected to neighboring mitochondria through narrow constrictions, suggesting impaired fission (Fields et al., 2002). However, in *Arabidopsis*, mutations in the CLU family gene *FRIENDLY* do not cause constrictions, but instead lead to increased association time during the mitochondrial fusion process, which was reported to favor clustering (El Zawily et al., 2014). In *Drosophila*, the CLU ortholog *clueless* interacts genetically (Cox and Spradling, 2009) and physically with the PINK1–Parkin pathway (Sen et al., 2015), to promote Valosin-Containing Protein (VCP)-mediated Marf degradation during the Parkin-dependent mitophagy (Wang et al., 2016). More recently, Gao et al. have reported that human CLUH interacts with a subset of mRNAs encoding mitochondrial proteins, suggesting that CLUH is also involved in mitochondrial biogenesis (Gao et al., 2014). Support for this role has also been provided by studies in *Drosophila*, which demonstrated that CLU is a ribonucleoprotein binding ribosomal components at the mitochondrial outer membrane (Sen and Cox, 2016). Clearly, further studies are needed to understand whether alteration in mitochondrial distribution in CLUH-depleted cells is a primary effect or secondary to mitochondrial biogenesis defects.

<sup>1</sup>Equipe MitoLab, Institut MitoVasc, Université d'Angers, UMR CNRS 6015, INSERM U1083, Angers, 49933 France. <sup>2</sup>SCIAM, Institut de Biologie en Santé, Université d'Angers, Angers 49933, France. <sup>3</sup>MRC Mill Hill Laboratory, London NW3 2PF, UK. <sup>4</sup>MitoStress team, IRHS, Université d'Angers, Agrocampus-Ouest, INRA, SFR QuaSaV, Beaucouzé 49071, France.

<sup>‡</sup>Authors for correspondence (guy.lenaers@inserm.fr; salim.khiati@univ-angers.fr)

DOI: 10.1242/jcs.201616

Taken together, these data revealed a broad involvement of CLU in mitochondrial physiology, which have been reinforced by bioinformatics analyses showing that *CLUH* is coexpressed with a set of genes involved in mitochondrial metabolic pathways and oxidative phosphorylation (OXPHOS) (Gao et al., 2014). However, despite having clear effects on mitochondrial distribution, it is unclear to what degree CLU function is involved in energy production and cellular metabolism. To gain insight into this question, we generated *CLUH*-knockout (KO) HeLa cells by using the CRISPR/Cas9 technique. Characterization of this *CLUH*-KO cell line revealed a decreased cell size with clustered mitochondria. In addition *CLUH*-KO cells showed abnormal cristae structures, OXPHOS defects resulting from altered mitochondrial translation, and drastic changes in metabolomic profiles.

## RESULTS

### **CLUH knockout in HeLa cells leads to clustered mitochondria and reduced cell size**

To characterize the impact of CLU on cellular metabolism, we generated *CLUH*-KO HeLa cells by using the CRISPR/Cas9 technique. Plasmids encoding for Cas9 and for the guide-RNA targeting *CLUH* exon4 were co-transfected with a puromycin-resistant gene flanked by homology arms upstream and downstream of the target site. A total of 23 colonies were screened by western blotting, among which three selected clones showed the absence of the *CLUH* protein (Fig. 1A; Fig. S1A,B). We then selected one cell line that had a reduction of at least 80% in the amount of *CLUH* transcript compared to that in wild-type (WT) cells, as determined by quantitative real-time reverse transcription PCR (qRT-PCR) (Fig. 1B). In addition, we checked that no detectable PCR product could be amplified from the genomic DNA when using primers hybridizing to *CLUH* exon 4 (Fig. 1C). Because CLU deficiency induces mitochondrial clustering in all models so far reported, we investigated mitochondrial distribution in *CLUH*-KO cells. Live confocal imaging of MitoTracker-stained cells showed that mitochondria were clustered around the nucleus in *CLUH*-KO cells (Fig. 1D; Fig. S1C). In addition, we observed that these cells had a drastically reduced size (Fig. 1E). To address an eventual correlation between the reduced cell size and the abnormal mitochondrial distribution, we standardized cell size using the CYTOO micropatterns (Fig. 1F; Fig. S1D). After 12 h, phase-contrast microscopy showed that both WT and mutant cells occupied the whole surface of square-shaped CYTOO micropatterns (Fig. 1F, left panels; Fig. S1D). While WT cells showed the expected even mitochondrial distribution throughout the cytoplasm (Fig. 1F, third panel), the KO cells showed mitochondria clustered around the nucleus, despite the cell growth over the whole available surface (Fig. 1F, right panel; Fig. S1D). Quantification of mitochondrial clustering, calculated as the amount of the mitochondrial surface divided by the whole cell area, revealed that 68% of *CLUH*-KO cells show clustered mitochondria, while only 28% of WT cells show this phenotype (Fig. S1E,F). Moreover, analysis of mitochondrial network morphology using Imaris Filament Tracer demonstrated that mitochondria were more connected in the KO cells (Fig. 1F, right panels), although, the resolution of our fluorescent microscopy observations cannot distinguish whether mitochondria are truly fused or simply apposed with each other. Because clustering of mitochondria might be related to cytoskeleton alterations, we investigated whether cell mobility, by a scratch test, and the response to paclitaxel, a microtubule-stabilizing drug, was affected in the KO cells.

Interestingly, the absence of *CLUH* decreased the ability to migrate and increased sensitivity to paclitaxel treatment (Fig. S2).

### **CLUH deficiency decreases the abundance of OXPHOS complexes following the inhibition of mitochondrial translation**

To gain further insights in the consequences of *CLUH* deficiency, we analyzed the expression of OXPHOS complex subunits with specific antibodies. Western blotting analysis showed that the amount of ATP5A (complex V), UQCRC2 (complex III), Cox II (complex IV) and NDUFB8 (complex I) subunits were all decreased in both whole-cell lysate and mitochondrial lysate of KO cells, while VDAC expression level remained constant in both conditions (Fig. 2A). We then explored respiratory complex assembly by using Blue Native (BN)-PAGE with specific antibodies for each complex (Fig. 2B). Interestingly, although the abundance of complex II, which is composed only of nuclear-encoded subunits, did not differ between WT and KO cells, the abundances of complexes I, III, IV and V, which are composed of subunits encoded by both nuclear and mitochondrial genes, were drastically decreased (by 50%, 80%, 40% and 20%, respectively) in KO cells (Fig. 2C). As these changes are frequently associated with a defect in the maintenance of the amount of the mitochondrial genome, we evaluated the integrity of the mtDNA. Indeed, as assessed by qPCR with two sets of primers targeting the nuclear and mitochondrial genome, we show that mtDNA amount was not affected in KO compared to the WT cells either at steady state or during recovery after ethidium bromide-mediated depletion (Fig. S3A,B). Moreover, as assessed by long-fragment PCR, we did not find any evidence for mtDNA deletions in KO cells (Fig. S3C). These results indicate that neither mtDNA quantity (Fig. S3B) nor quality (Fig. S3C) was compromised in KO cells. Thus, we further investigated the status of mitochondrial translation. To do this, we first performed an *in silico* co-expression analysis of *CLUH* using the NCI-60 database (Fig. 2D) and the CellMiner tool (<http://discover.nci.nih.gov/cellminer/>) (Langer et al., 2010; Liu et al., 2010; Reinhold et al., 2012). The 258 genes that positively correlate with the *CLUH* mRNA expression level (correlation factors between 1 and 0.5; Table S1) were classified by using the functional annotation database PANTHER (<http://pantherdb.org>). Based on PANTHER sorting classifications to molecular function and biological process (Mi et al., 2013), the 258 genes are mainly involved on mitochondrial function (Fig. 2D). However, beside genes involved in mitochondrial metabolic pathways and cellular respiration previously reported (Gao et al., 2014), the ontology-based analysis revealed that genes involved in mitochondrial translation are also highly correlated with *CLUH* expression, being enriched by 14 times (Fig. 2D). To corroborate this analysis, we analyzed the products of mitochondrial translation by pulsing cells with radioactive [<sup>35</sup>S]methionine in the presence of emetine, an inhibitor of cytoplasmic translation. We found that mitochondrial translation was significantly decreased in KO cells (Fig. 2E). Indeed, despite the equal total protein loading shown by Coomassie staining (Fig. 2E, right panel), the autoradiography shows a clear decrease in the abundance of mitochondrial radiolabeled proteins in KO versus WT cells (Fig. 2E, left and middle panel). This defect could be due to the decrease in mitochondrial protein synthesis machinery, as western blots of mitochondrial fractions revealed that the small MRPS27 and MRPS17, and the large MRPL44 and MRPL13 ribosomal subunits, the ERF1 translation assembly factor and EFG1 (also known as GFM1) and TUFM elongation factors were decreased in KO versus WT cells (Fig. 2F). Taken together, these results indicate



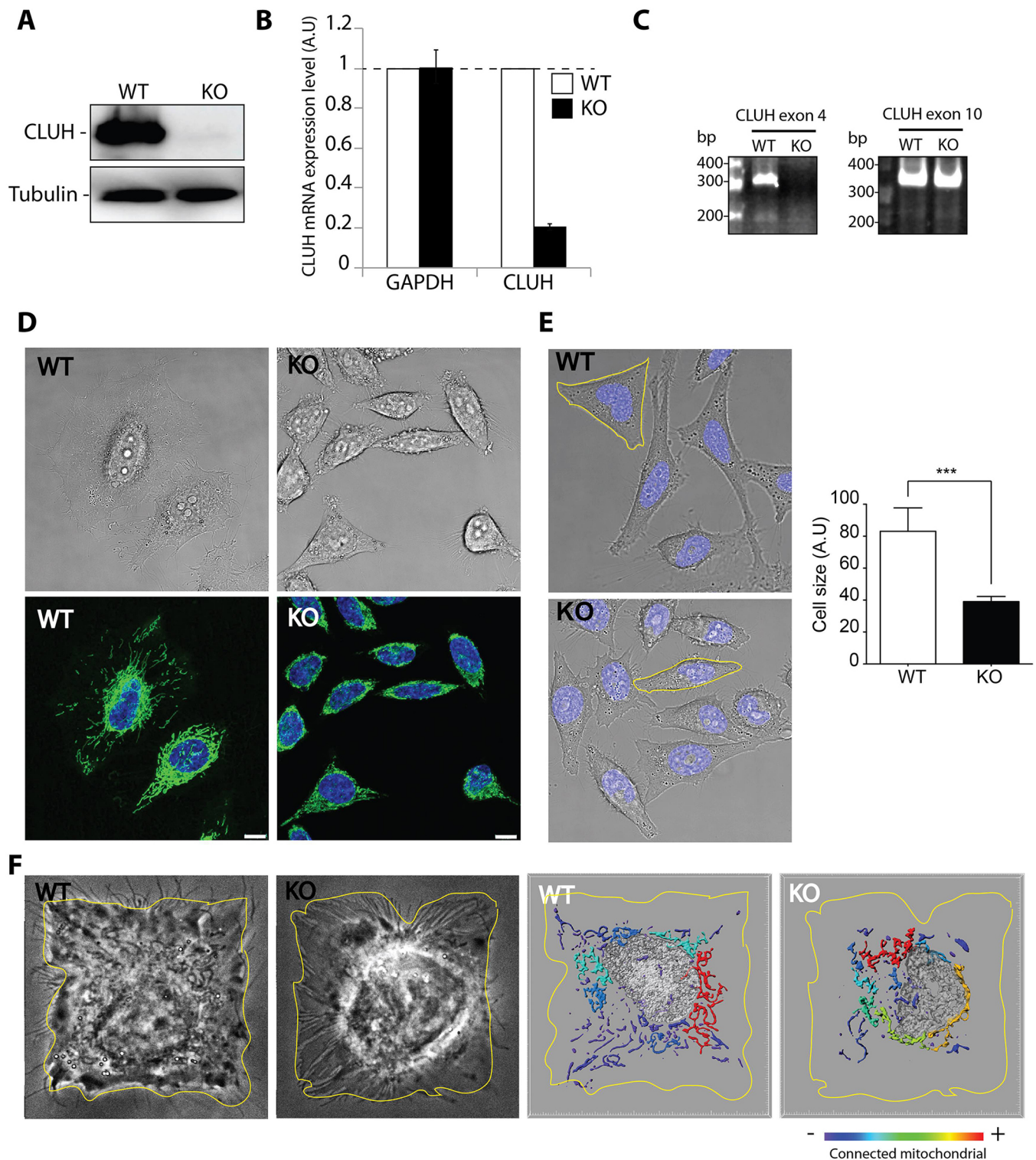


**Fig. 1. Generation of CLUH KO cells and characterization of mitochondrial distribution.** (A) Generation of CLUH-KO HeLa cells by using a CRISPR/Cas9 technique. Western blotting of whole-cell lysate using CLUH-specific antibody, showing lack of CLUH protein in these cells. Tubulin was included as a loading control. (B) Relative *CLUH* mRNA expression levels (A.U., arbitrary units) in WT and CLUH-KO HeLa cells in four independent experiments (mean  $\pm$  s.e.m.). (C) Representative gel of the *CLUH* exon 4 (targeted by Cas9) PCR product; *CLUH* exon 10 was used as a loading control. (D) Live-cell light (top panels) and fluorescence (lower panels) images of cells stained with MitoTracker Green in WT (left) and CLUH-KO (right) cells. Scale bar: 1  $\mu$ m. (E) Left panels, live-cell light and fluorescence (DAPI) images. Right panel, quantification of cell size as determined by measuring cell areas, as highlighted with the yellow line in the images, with ImageJ. Results are mean  $\pm$  s.e.m. for 200 cells measured in each condition and in three independent experiments. \*\*\* $P \leq 0.001$  (two-tailed paired *t*-test). (F) Live-cell phase contrast images (left two panels) and surface reconstitution of fluorescence images (right two panels) of individual WT and KO cells in CYTOO square-shaped micropatterns. Experiments were replicated four times in the laboratory. Mitochondria were stained with MitoTracker green and color encoded using Imaris software (Bitplane, Zurich, Switzerland) according to their length. Imaris filament tracer colors code indicate mitochondrial network shapes: red for long mitochondria and purple for fragmented mitochondria. All the experiments were replicated four times in our laboratory.

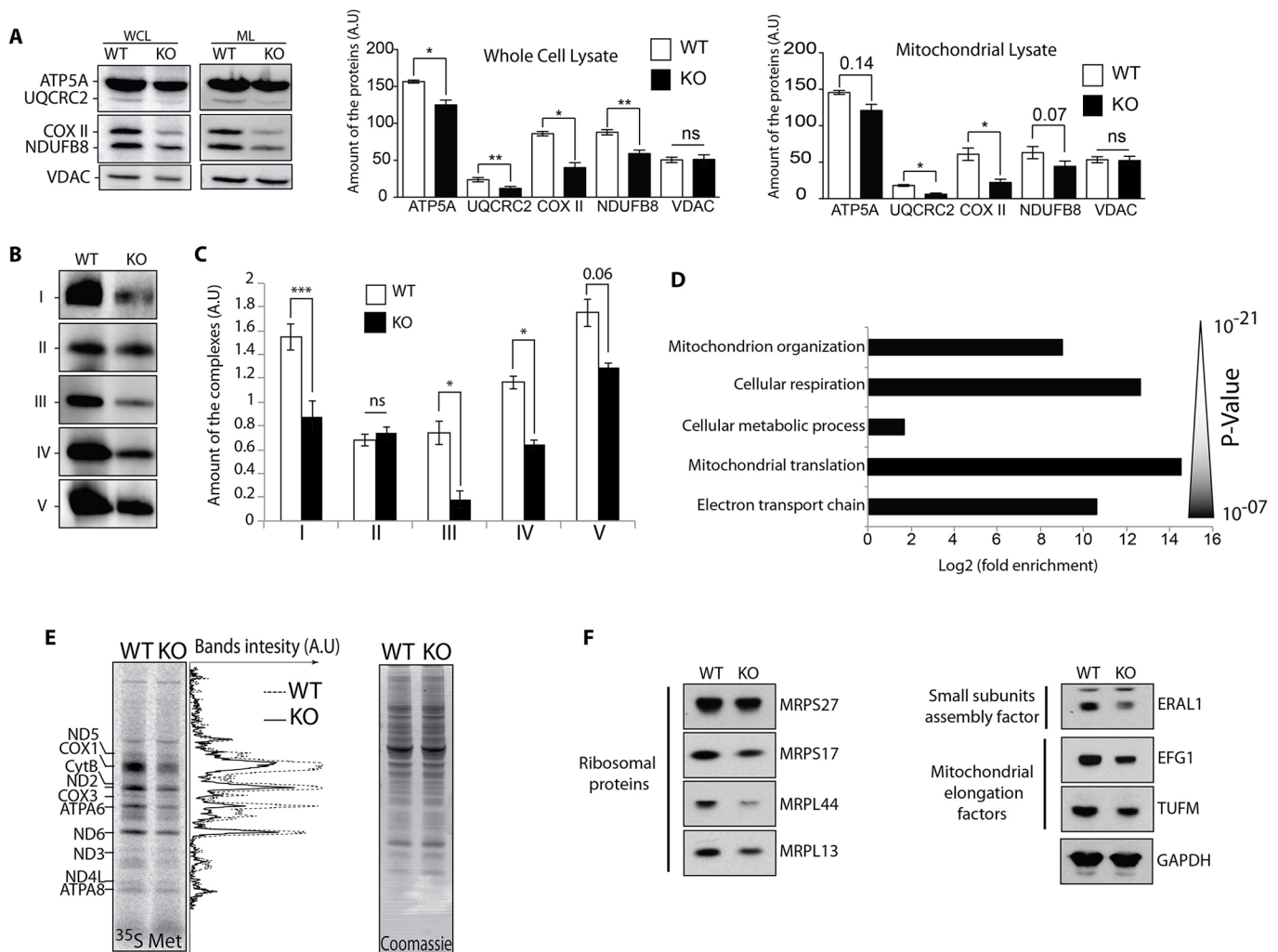


**Fig. 2. Mitochondrial OXPHOS complex abundance and mitochondrial translation are decreased in CLUH-KO cells.** (A) Left panel, western blots showing, with specific antibodies, the expression level in whole-cell lysates (WCL) and in mitochondrial lysate (ML) of ATP5A (complex-V), UQCRC2 (complex III), Cox II (complex IV) and NDUFB8 (complex I) subunits. VDAC expression level was used as a loading control. Right panels, quantification of the amounts of OXPHOS complex subunits (mean±s.e.m.; A.U., arbitrary units) of four independent experiments. (B) BN-PAGE analysis of the five OXPHOS complexes with specific antibodies for each complex. (C) Quantification of amounts of OXPHOS complexes in the BN-PAGE analysis. Results are mean±s.e.m. for four independent experiments. \* $P<0.05$ ; \*\*\* $P<0.001$  (two-tailed paired  $t$ -test). (D) DAVID gene ontology analysis of the 258 genes positively and highly correlated with CLUH mRNA expression level as determined by an *in silico* co-expression analysis using the CellMiner tool and the NCI-60 database. The 258 genes were sorted using the functional annotation database PANTHER (<http://pantherdb.org>), which are presented with fold enrichment according to biological processes and  $P$ -values. (E) Mitochondrial translation products were labeled with [<sup>35</sup>S]methionine in the presence of emetine, a cytoplasmic translation inhibitor. The left panels show the autoradiography of the radiolabeled newly synthesized mitochondrial proteins, while the right panel shows the Western blots, demonstrating equal protein loading of WT and KO cell lysates. All the experiments were replicated four times in our laboratory. (F) Western blots of cell lysates using specific antibodies show that CLUH-KO have a lower amount of mitochondrial small MRPS27 and MRPS17 and large MRPL44 and MRPL13 ribosomal subunits, translation assembly factor ERL1 and mitochondrial elongation factors EFG1 and TUFM. GAPDH was used as loading control.

that in addition to mitochondrial mislocalization, mitochondrial translation and OXPHOS complex assembly are significantly decreased in CLUH-KO cells.

#### CLUH deficiency leads to altered mitochondrial ultrastructure and impaired respiratory activities

OXPHOS complexes contribute to the shape of the inner membrane, particularly the ATPase which is involved in cristae formation (Davies et al., 2012). To determine whether decreased abundance of OXPHOS complexes in CLUH-KO cells parallels mitochondrial ultrastructure defects, we performed transmission electron microscopy (TEM) on WT and CLUH-KO cells (Fig. 3A). KO cells contained two populations of mitochondria that could be distinguished on the basis of their ultrastructure: one population

contained a few disorganized cristae and an electron-light matrix (Fig. 3A, yellow arrowheads) and the second population had enclosed small mitochondria and displayed an electron-dense matrix with many cristae (Fig. 3A, red arrowheads). These populations represent 40% and 60% of total mitochondria, respectively (Fig. S4). Moreover, we observed that some mitochondria, 2% of quantified mitochondria, were connected in KO cells by thin tubules (Fig. 3A, black arrow) suggesting a failure of membrane to fully divide or to fuse. We next chose to investigate OXPHOS complex activities in isolated mitochondria from WT and KO cells (Fig. 3B). All activities were normalized to the Krebs cycle enzyme citrate synthase, which is used as a reference for mitochondrial mass. The activities of complexes I, IV and V were each decreased in KO cells by 40% (Fig. 3B), while complex II



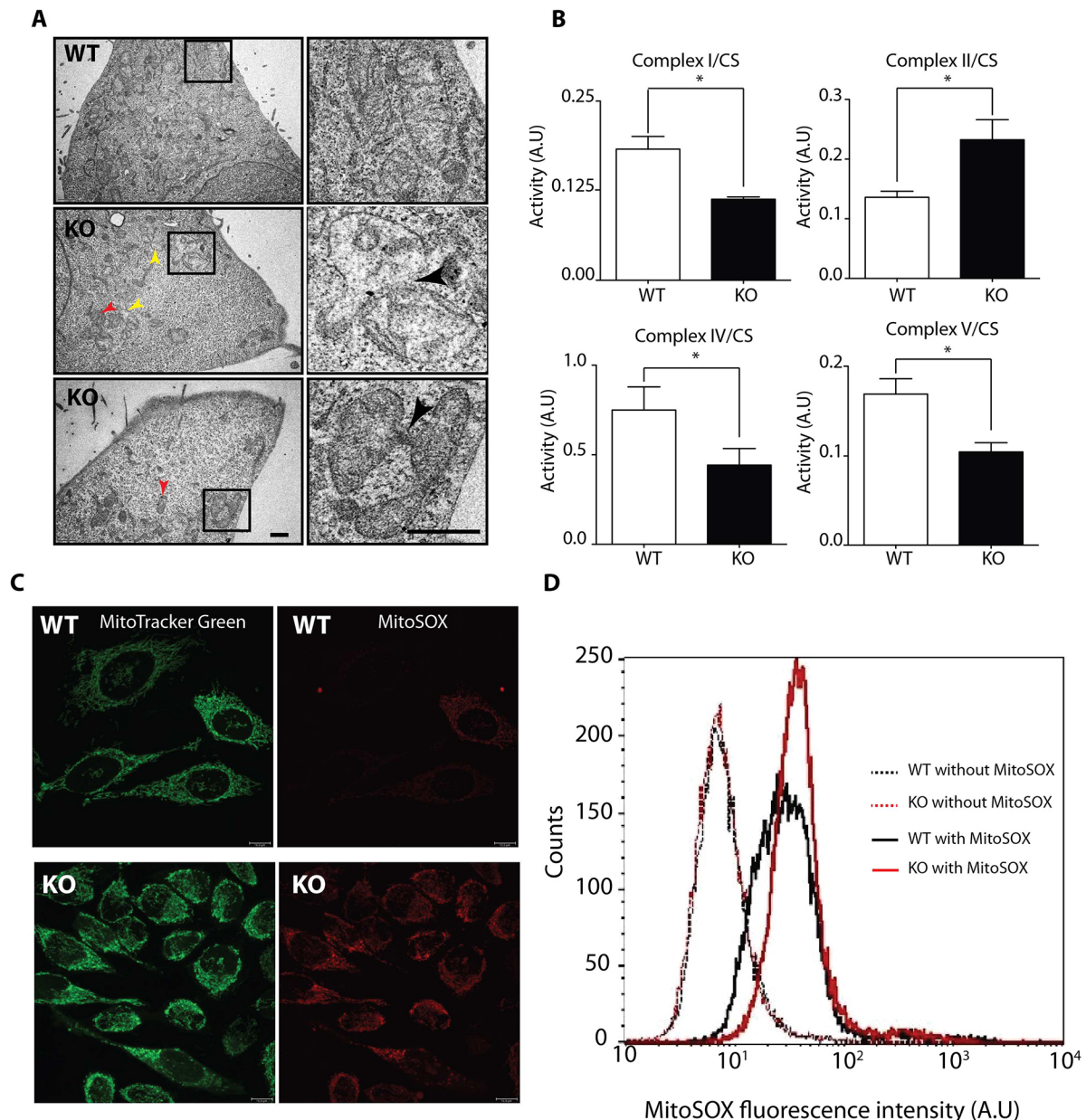


**Fig. 3. Mitochondrial ultrastructure and activities are defective in CLUH KO cells leading to ROS overproduction.** (A) Representative TEM images of WT and two independent CLUH-KO cells (left). 50 cells were analyzed in each condition. Enlarged views of the boxed areas (right) show the mitochondrial ultrastructure. Yellow arrowheads indicate disorganized cristae, while red arrowheads indicate homogeneous dense cristae. Right, black arrowheads indicate connected mitochondria. Scale bars: 500 nm. (B) Activities of OXPHOS complexes I, II, IV and V in WT and CLUH KO cells subunits (A.U., arbitrary units). Data were normalized to citrate synthase (CS) activity. Results are mean  $\pm$  s.e.m. for four independent experiments. \* $P < 0.05$  (two-tailed paired *t*-test). (C) Representative images of mitochondria from WT and CLUH KO cells stained with MitoTracker Green (left panels) and MitoSOX (right panels). (D) FACS analysis of WT and KO cells after MitoSOX staining. All the experiments were replicated four times in our laboratory.

activity in KO cells was increased compared to that seen in control cells (Fig. 3B), in agreement with our measurements of complex abundance (Fig. 2). In general, alterations of mitochondrial respiration lead to the generation of reactive oxygen species (ROS); thus, we investigated mitochondrial ROS generation by means of live-cell imaging following incubation with the superoxide indicator MitoSOX Red, whose fluorescence increases with mitochondrial ROS production (Mukhopadhyay et al., 2007). Only weak fluorescence was detected in WT cells, while the CLUH-KO cells clearly displayed increased fluorescence localized to mitochondria, indicating increased ROS production (Fig. 3C). FACS analysis (Fig. 3D) confirmed that 1 h after MitoSOX staining,

KO cells showed higher fluorescence intensity compared to that seen in WT cells (Fig. 3D). Taken together, these results demonstrate that the mitochondria from CLUH-KO cells display pronounced ultrastructural defects affecting cristae formation, reduced OXPHOS abundance and activity, and concomitant increased ROS production.

#### CLUH deficiency increases the glycolytic rate

To assess the consequences of the respiratory dysfunctions in CLUH-KO cells on the energetic metabolism, we next evaluated parameters associated with glycolysis. KO cells consumed glucose at a faster rate than WT cells (Fig. 4A), such that after 2 and 4 days

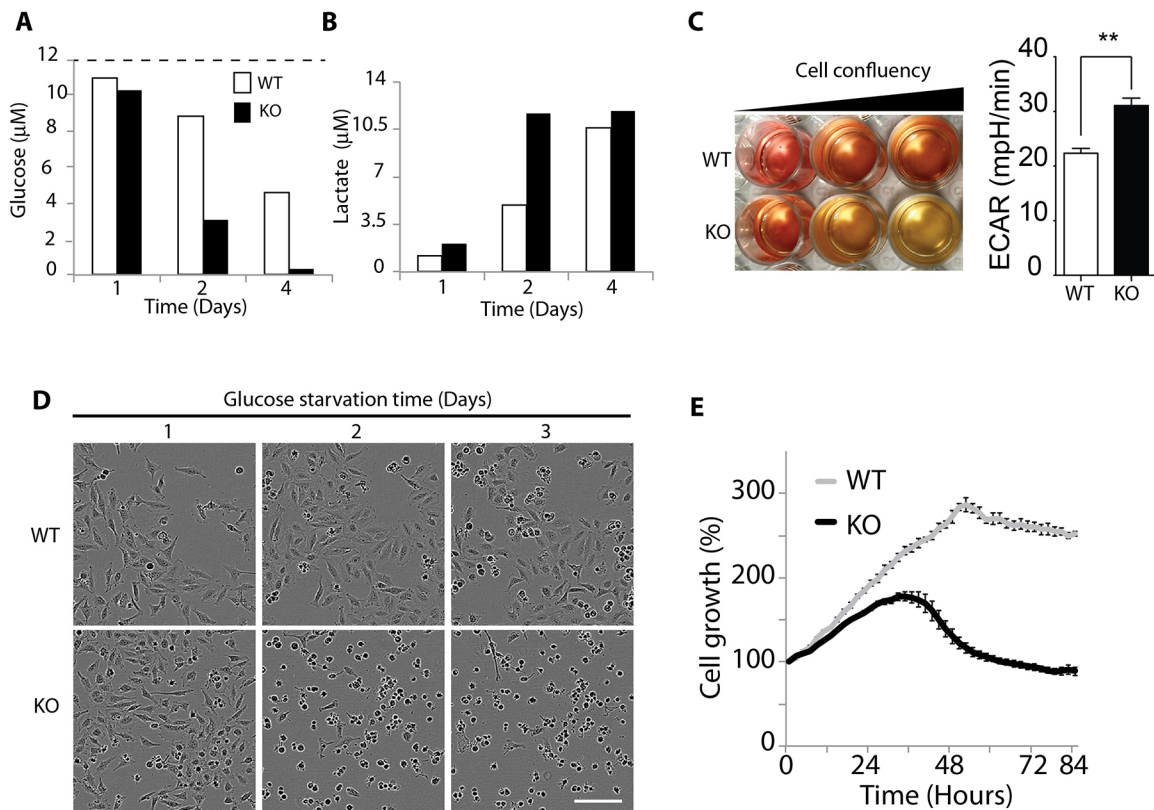


**Fig. 4. KO cells shift their metabolism to glycolysis, with increased glucose dependency.** Measurements of glucose (A) and of lactate (B) concentrations in medium after 1, 2 and 4 days of cell culture. (C) Left panel, color shift from red to yellow of the medium after 24 h of culture of WT and KO cells, seeded at increasing confluences. Right panel, ECARs measurements with a Seahorse machine. Results are mean±s.e.m. for four independent experiments. \*\* $P<0.005$  (two-tailed paired  $t$ -test). (D) Representative real time images, using IncuCyte, after maintaining WT and CLUH KO cells for 3 days without glucose. Scale bar: 150 μm. (E) Quantification (mean±s.e.m.;  $n=4$ ) of cell growth using IncuCyte, during glucose starvation for 84 h. All the experiments were replicated four times in our laboratory.

of culture only 25% and 4%, respectively, of the original glucose remained in the medium of KO cells, while 75% and 40%, respectively, of the original glucose remained in that of WT cells. In addition, measurement of extracellular lactate revealed that KO cells produced two times more lactate than WT cells (Fig. 4B), which correlated with the acidification of the medium, as indicated by the change from red to yellow for the Phenol Red indicator. In parallel, the extracellular acidification rate (ECAR), which is predominately the result of glycolysis, was increased in KO cells compared to that seen for the WT cells (Fig. 4C). Finally, we investigated cell growth and death after glucose starvation by using the IncuCyte ZOOM system, in which cell density and shape are monitored by photonic microscopy while cells are maintained under standard culture conditions (Fig. 4D). As assessed by using an adapted confluence mask, cell viability was determined and the percentage of cell growth was calculated based on the change of cell confluency over a time course. Our analysis showed that at 24 h after glucose starvation, KO cell growth was drastically slower than that of WT cells (Fig. 4E). In addition, they started dying after 36 h of starvation and were all dead by 72 h, while WT cells grew normally for 2 days and were still alive after 3 days of starvation. Taken together, these results demonstrate a metabolic shift in CLUH-KO cells, increasing glycolysis and glucose dependency.

#### CLUH deficiency modulates cellular metabolic steady state

Mitochondria are crucial contributors to many metabolic pathways, such as those leading to the anabolism of amino acids, hormones and phospholipids. Whether these pathways are compromised by

alterations of mitochondrial structure and distribution is an open question. Thus, we performed a targeted metabolic analysis using the AbsoluteIDQ p180 kit (Biocrates, Innsbruck, Austria) to obtain a global view of the effects of CLUH function on cell metabolism. Metabolites, including acylcarnitines ( $n=40$ ), amino acids ( $n=21$ ), biogenic amines ( $n=21$ ), monosaccharides ( $n=1$ ), sphingolipids ( $n=15$ ) and glycerophospholipids ( $n=90$ ), were measured by mass spectrometry (AB Sciex QTRAP 5500, Life Sciences SCIEX, Villebon sur Yvette, France). Flow-injection analysis tandem mass spectrometry (FIA-MS/MS) was used to quantify acylcarnitines, glycerophospholipids, sphingolipids and sugar, whereas liquid chromatography tandem mass spectrometry (LC-MS/MS) allowed the quantification of amino acids and biogenic amines. Cellular extractions from ten independent flasks for both WT and KO cells were used for this analysis, and the metabolite concentrations were normalized with respect to protein cell extract concentrations. Multivariate data analysis showed a significant ( $Q_{2cum}=0.92$ ) separation between WT and CLUH-KO cells, as represented in an orthogonal partial least squares discriminant analysis (OPLS-DA), a supervised multiple regression analysis, score plot (Fig. 5A). The volcano plot of the metabolites whose concentrations significantly changed after knocking out of CLUH revealed an increase of polar metabolites and a decrease of phospholipids in KO compared to the WT cells (Fig. 5B). Indeed, the amount of non-essential amino acids (Fig. 5C,D), carnosine (Fig. 5E) and palmitoylcarnitine (Fig. 5F) were increased by two to three times in KO compared to in the WT cells (Fig. 5C,D), with the polyamines, including spermine, spermidine and putrescine (Fig. 5G), increased by 76%, 37% and

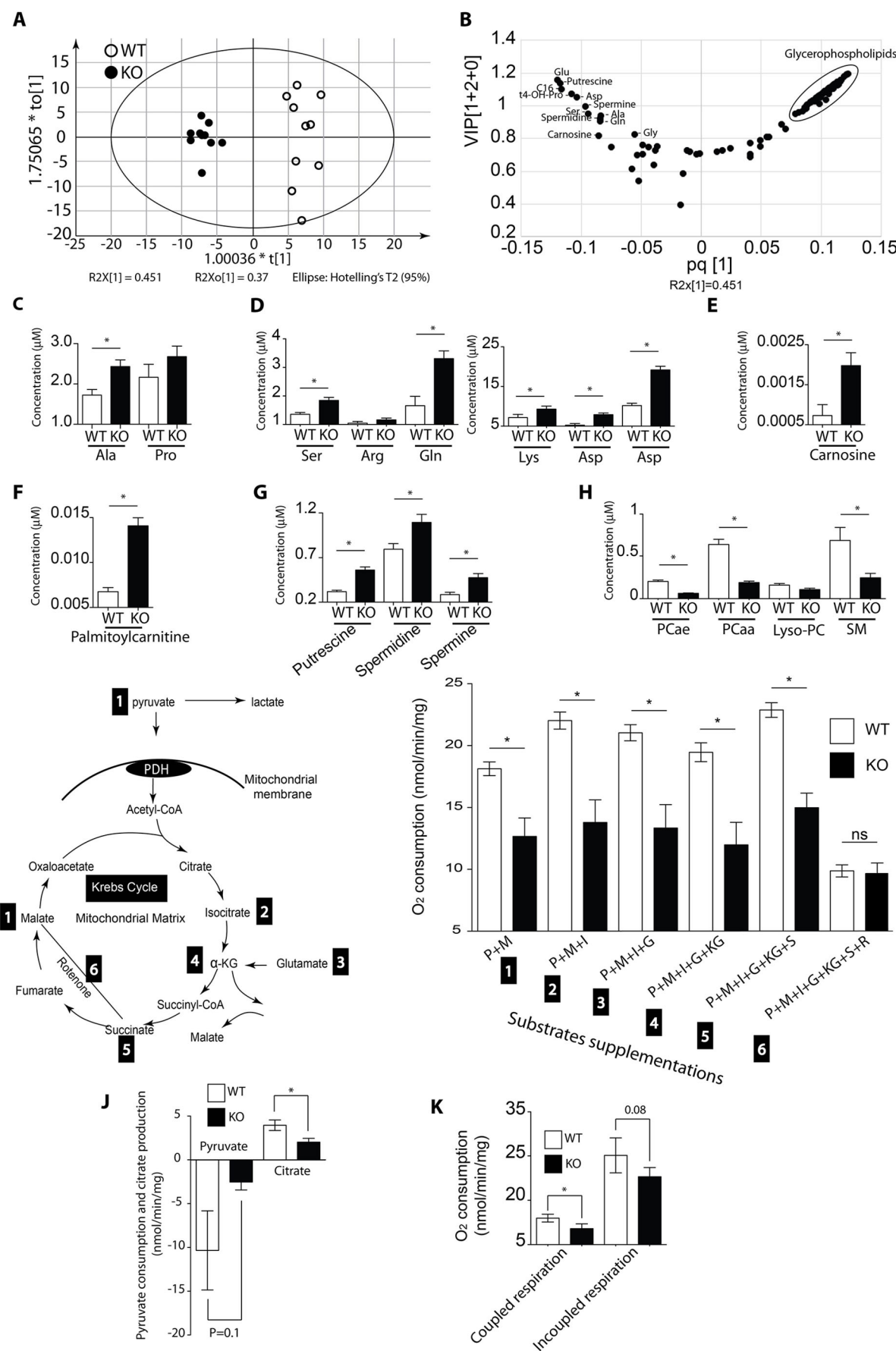


Fig. 5. See next page for legend.



**Fig. 5. CLUH deficiency modulates the cellular metabolic steady state.**

(A) The orthogonal partial least squares discriminant analysis (OPLS-DA) model comparing ten cultures of WT and CLUH KO cells shows a clear distinction between the two groups. (B) Volcano plot showing the distribution of the quantified metabolites. (C–H) Bar plots represent the mean  $\pm$  s.e.m. ( $n=10$ ) relative concentrations of the metabolites. (C) Alanine (Ala) and proline (Pro); (D) serine (Ser), arginine (Arg), glutamine (Gln), lysine (Lys) and aspartate (Asp); (E) carnitine; (F) palmitoylcarnitine; (G) putrescine, spermidine and spermine; (H) phosphatidylcholine (PCae and PCaa), lyso-phosphatidylcholine (Lyso-PC) and sphingomyelins (SM). \* $P<0.05$  (two-tailed paired  $t$ -test). (I) Respirations rates (mean  $\pm$  s.e.m.,  $n=4$ ; right panel) in permeabilized cells after supplying different substrates of Krebs cycles sequentially, as indicated by numbers in the scheme (left panel). The added substrates were: pyruvate and malate (1), isocitrate (2), glutamine (3),  $\alpha$ -ketoglutarate (4) and succinate (5). Rotenone, a complex I inhibitor, was added at the end of the experiment (6). \* $P<0.05$ ; ns, not significant (two-tailed paired  $t$ -test). (J) Consumption of pyruvate and production of citrate in WT and KO cells were measured (mean  $\pm$  s.e.m.,  $n=4$ ) using mass spectrometry analysis. Metabolites were followed for 30 min in medium after stimulation of the phosphorylating respiration to 50% of the maximal mitochondrial respiratory rate ( $V_{max}$ ) in WT and KO cells. Pyruvate and citrate amounts metabolized per minute were normalized to protein concentrations (mg). \* $P<0.05$  (two-tailed paired  $t$ -test). All the experiments were replicated four times in our laboratory. (K)  $\beta$ -oxidation was investigated by following the respirations rates in permeabilized cells after supplying carnitine, malate and palmytoyl-CoA (mean  $\pm$  s.e.m.,  $n=4$ ). All the experiments were replicated four times in our laboratory.

66%, respectively. Conversely, all lipids were less abundant in KO cells, including phosphatidylcholine, lyso-phosphatidylcholine and sphingomyelin, which were decreased by 70%, 32% and 64%, respectively (Fig. 5H). These different metabolic signatures highlight the profound changes in cell metabolism that result from CLUH deficiency, and indicate the central role of CLUH in orchestrating cellular metabolism. Because increased concentrations in amino acid in KO cells could reflect a defective Krebs cycle, we evaluated the respiration rates in permeabilized cells after supplying different substrates of the Krebs cycle (Fig. 5I). We observed that in the presence of pyruvate and malate, respiration rates were significantly decreased in KO cells (Fig. 5I). Moreover, mass spectrometry analysis revealed that KO cells consume less pyruvate and produce less citrate than do WT cells (Fig. 5J). Next, we observed that the addition of isocitrate failed to increase the respiration rate in KO cells, while it did in WT cells (Fig. 5I). Similar results were obtained after the sequential addition of glutamine,  $\alpha$ -ketoglutarate and succinate (Fig. 5I).

Finally, to evaluate the  $\beta$ -oxidation, we measured the respiration rates in permeabilized cells after supplying carnitine, malate and palmytoyl-CoA. Again, coupling and uncoupling respirations were slower in KO cells compared to that seen in WT cells (Fig. 5K). Taken together, these results indicate that in CLUH-KO cells, both the Krebs cycle and the  $\beta$ -oxidation are defective, leading to a profound remodeling of cellular metabolism.

**DISCUSSION**

In most eukaryotic cells, mitochondria appear as a reticulated network spread out all over the cytoplasmic volume in order to locally fulfill the energetic requirements. This strongly suggests that in the eukaryote ancestor that preceded the branching of the present eukaryote phyla, one of the main challenges in the generation of an efficient mitochondrial network consisted of the elaboration of a mechanism allowing proper mitochondrial distribution. In this respect, CLUH, a highly evolutionary conserved protein throughout the eukaryotic kingdom, is a key element, as its deletion leads to mitochondrial clustering in all models so far considered. To gain

insights into CLUH functions, we generated a homozygous deletion of *CLUH* in HeLa cells by using the CRISPR/Cas9 technique. The data presented here confirmed that the absence of CLUH leads to mitochondrial clustering in HeLa cells. However, importantly, our results connect CLUH to altered mitochondrial ultrastructure, translation, respiration and major changes in cellular metabolism.

We first identified a clear reduction of cell size and volume, although no modification of the cytoskeleton was evident. This observation parallels the fact that in the *A. thaliana* plant model, deletion of *FRIENDLY*, the *CLUH* ortholog, leads to a global reduction of leaf, root and branch sizes (El Zawily et al., 2014). Similarly, knockout of *clueless* in *Drosophila* leads to sterile adults with reduced size, and uncoordinated movements, abnormal wing position and short life expectancy (Cox and Spradling, 2009).

As expected, observation of mitochondria in CLUH-KO cells revealed clustered networks, but with heterogeneous mitochondria displaying two phenotypes, one with a normal structure and dense matrix, and one with altered cristae structures and a light matrix. The peculiar mitochondrial phenotype had already been observed in adult muscles from the *Drosophila clueless* strain (Sen et al., 2015) but was absent in COS7 cells in which CLUH expression was silenced using siRNA (Gao et al., 2014), suggesting that stable CLUH-KO clones trigger adaptation processes that are not set in an acute model triggered by siRNA. The existence of two mitochondrial populations in KO cells could be related to the physical and functional interactions between CLUH and the PINK–Parkin pathway, which promote the turnover of mitochondria to eliminate any that are defective (Cox and Spradling, 2009; Sen et al., 2015; Wang et al., 2016). Indeed, a cross-talk between CLUH and mitophagy in *Drosophila* was found to be associated with the degradation of the valosin-containing protein Mitofusin (Marf), in order to prevent the fusion between healthy and altered mitochondria (Wang et al., 2016). This concept could support why some thin connections between mitochondria are observed in CLUH-KO cells, as already reported in the *cluA*<sup>−</sup> mutant of *Dictyostelium* (Fields et al., 2002), which might result from aborted fusion or defective fission. However, electron microscopy observations did not reveal an increase in mitochondrial size, excluding the possibility that there is a major modification of the equilibrium between mitochondrial fusion and fission.

Recently, a *Cluh* knockout mouse was generated, and its characterization showed the importance of CLUH in the regulation of nuclear mRNAs encoding mitochondrial proteins, which are required for metabolism reprogramming during nutriment deprivation. Indeed, although the fetal development was normal in *Cluh*-KO mouse, pups died at 0–1 days after birth, and liver analysis at embryonic day (E)18.5, or at 8 weeks for a liver-specific *Cluh* KO mouse, revealed severe metabolic alterations under starvation conditions (Schatten et al., 2017). Thus, both HeLa cells and mice deleted for *Cluh* revealed clustered mitochondria and hypersensitivity to glucose starvation. However, the worst mitochondrial ultrastructure defects were observed only after nutriment deprivation in the mouse model, suggesting that CLUH is important for specific metabolic statuses. Our data extend these results by showing that CLUH exerts a broader role in maintaining the whole cellular metabolism, as we found mitochondrial defects and changes in many metabolites, even in normal growth conditions. Thus, both *in vitro* and *in vivo* models revealed that CLUH has an essential role in the coordination of the cellular metabolism.

In parallel, we find that *CLUH*-KO cells have a significant proportion of mitochondria with altered inner structures. This cristae

disorganization may be linked to the reduced abundance of the respiratory complex subunits and their assembly into the respirasome, and might explain why we found that the respiratory complexes had reduced enzymatic activities and that there was an increase in ROS production. Frequently, a decrease in the abundance of the respiratory subunits and complex assembly is associated with mtDNA depletion, which was found in the liver and heart of *Cluh*-KO mice, but not in their kidney and brain tissues (Schatton et al., 2017). In our cellular model, the mtDNA abundance remained unaffected, but the mitochondrial protein synthesis was significantly reduced in the absence of CLUH, suggesting a major alteration of the mitochondrial translation process. Beside the importance of CLUH on mRNA translation of nuclear-encoded mitochondrial proteins (Gao et al., 2014; Sen and Cox, 2016), the evidence that PINK1 and Parkin also control the mRNA translation of the respiratory chain subunits at the outer mitochondrial membrane (Gehrke et al., 2015) suggests that a concerted regulation of all the respiratory components encoded by the nuclear and mitochondrial genomes can be achieved by a crosstalk between CLUH and the PINK–Parkin pathway. Thus, the decrease in the mitochondrial translation machinery in CLUH-KO cells without mtDNA defects raises questions about both the stability of mitochondrial mRNA and the regulation of specific downstream effects on the mRNAs that are targeted by CLUH (Schatton et al., 2017).

To further address the consequences of the absence of CLUH on mitochondrial physiology, we characterized the energetic and metabolic status of these KO cells. We first observed a metabolic reprogramming, switching the energetic production from OXPHOS to a predominant glycolysis process, and revealing a high dependency on glucose fueling. In parallel, by using targeted mass spectrometry, we found a drastic change in the metabolomics signature. Multivariate analysis of our results showed that there was a significant increase in polar metabolites, including the non-essential amino acids, carnosine, palmitoylcarnitine and polyamines, and a dramatic decrease in the amounts of some lipids. The increase in carnosine ( $\beta$ -alanyl-L-histidine), which has an antioxidant effect (Kohen et al., 1988), might protect cells from the increased ROS production induced by the defective mitochondria in KO cells. We also found an increase of many amino acids, including alanine, glycine, serine, arginine, proline, glutamine, glutamate and aspartate, as also reported by Schatton et al. in the liver of E18.5 *Cluh*-KO embryo and in the serum of *Cluh*-KO mice that had been starved for 8 weeks (Schatton et al., 2017). This can be related to the dysfunction of the Krebs cycle, as we observed decreased respiration rates when supplying different substrates of the Krebs cycle. This could also be related to a reduced anabolic status and protein synthesis, paralleling the reduction of the cell size. Taken together, these results indicate that CLUH-KO cells can not support normal respiration and are unable to supply the Krebs cycle with its intermediates.

In addition, we observed an increase in the palmitoylcarnitine level in CLUH-KO cells that might be due to a  $\beta$ -oxidation defect, as the mitochondrial carnitine system is essential for oxidation of long-chain fatty acids by catalyzing their transport into the mitochondrial matrix. This result is in contradiction with that of Schatton et al., who reported a decrease of palmitoylcarnitine levels in liver lysates of starved *Cluh*-KO mice at E18.5, although CPT2, the first enzyme in the long fatty  $\beta$ -oxidation, which generates acyl-carnitines (Lee et al., 2015), and HADHA, the enzyme required for the three last steps of mitochondrial  $\beta$ -oxidation were decreased in the liver tissues. To conciliate these opposite results, we propose that the differences in the biological origins of the samples analyzed and

their energetic environment may explain this discrepancy in the palmitoylcarnitine metabolism.

In addition, we found an increase in polyamines, such as putrescine, spermidine and spermine, which may be an adaption to allow survival of the CLUH-KO cells, as increased organic cations can restore conditions supporting cellular growth and viability (Nishimura et al., 2002; Pendeville et al., 2001). Finally, our metabolomics analysis disclosed dramatic decreased amounts of phospholipids in CLUH-KO cells, which could either be related to the smaller cell size and a lower protein to lipid ratio, or to altered mitochondrial metabolism of lipid precursors. These results could further explain the 10–15% decrease in the body weight of the *Cluh*-KO mice.

Taken together, our study shows that, through its crucial involvement in mitochondrial distribution, CLUH is central to a network of many functions related to mitochondrial quality control, mitochondrial ultrastructure, respirasome synthesis, energy production and metabolic pathways that maintain a sustainable cellular homeostasis. Finally, how the different evolutionary conserved domains of CLUH contribute to these multiple functions remains a challenge to address in the future.

## MATERIALS AND METHODS

### Generation of CLUH-KO HeLa cells via CRISPR/Cas9

HeLa were obtained from American Type Culture Collection and cultured in growth medium [Dulbecco's modified Eagle's medium (DMEM); Gibco] supplemented with 10% heat-inactivated fetal bovine serum (FBS; ThermoFisher) and 1 mM of sodium pyruvate and glutamine (ThermoFisher). Cells were verified by PCR and shown to be free of contamination with mycoplasma. Plasmids pX330 encoding for Cas9 and the guide-RNA targeting CLUH exon 4 (target site sequence: 5'-GTCTTACCGACGCGACCTGGG-3'), were co-transfected with a puromycin-resistant gene flanked by homology arms upstream and downstream of the target site. Transfected cells were selected with 1  $\mu$ g/ml puromycin at 72 h after initial transfection. Secondary screen by western blotting was carried out in 23 colonies to identify clones with different levels of CLUH expression. Three independent selected clones showed undetectable level of CLUH (Fig. S1A,B). PCR with primers upstream (forward primer, 5'-ATGTCCGAGACCTGCTCAAG-3') and downstream (reverse primer, 5'-GTCCATCTCCAAGCCCTTCT-3') of the target site confirmed the absence of the band in KO cells. For the exon 10 PCR, forward primer 5'-CGTCCGAGACCACTACA-3' and reverse primer 5'-AGCAGAGCTCCACCTCCT-3' were used. Clone 2 was used as knockout clone in subsequent experiments.

### qRT-PCR analysis

$10^6$  cells were harvested and suspended in 100  $\mu$ l phosphate-buffered saline (PBS), and total RNA was purified by using an RNeasy Mini Kit (cat no. 74104, Qiagen) according to the manufacturer's protocol. 2  $\mu$ g of RNA were reverse transcribed and qRT-PCRs were performed in triplicate in 96-well reaction plates (Applied Biosystems). Each reaction (final volume 10  $\mu$ l) contained 100 ng of cDNA, 5  $\mu$ l of Power SYBR-Green PCR Master Mix (Applied Biosystems) and 0.5  $\mu$ M of each forward and reverse primer. Two sets of primers were designed to measure mRNA expression level of CLUH. Primers sequences were: forward 1, 5'-GTGGAGCACAGGTACCTCCTC-3' and reverse 1, 5'-AGGGTCTGCTGTGCCGTC-3'; and forward 2, 5'-CACACGGGGCTTTTACCTGAATC and reverse 2, 5'-CAATCCATGG CATGCTCCGC-3'. *GAPDH* was used as the control.

### Live-cell confocal imaging

HeLa cells were seeded at the density of 20,000 cells/well in four-well glass-bottom  $\mu$ -slides (80427, Ibidi) for 24 h; then mitochondria and nuclei were stained using MitoTracker Green (ThermoFisher, M7514) and Hoechst 33342 (ThermoFisher) solutions at 100 nM, 30 min before confocal live-cell imaging. To measure mitochondrial reactive oxygen species (ROS), cells were stained with MitoSOX (ThermoFisher, M36008) at 5  $\mu$ M, 30 min

prior to imaging. All the images were captured using a Leica TCS SP8 confocal microscope with a 40×1.20 NA water objective lens (Leica Microsystems) equipped with a GaAsP Hybrid detector (HyD), at 37°C. For FACS analysis, MitoSOX at 5  $\mu$ M was added for 1 h.

In order to standardize cell size, HeLa cells were seeded at the density of 60,000 cells on CYTOO chips with square or T micropatterns. Images were acquired with the inverted widefield NIKON Ti-E microscope equipped with an Andor NEO sCOMS camera controlled by NIS Element software. Each image was obtained with a 100× oil objective (Nikon Plan Apo100×, N.A. 1.45). On average, 21 image planes were taken along the z-axis at 0.2  $\mu$ m increments. To limit mitochondrial movements, the images were taken at a controlled temperature (25°C). Huygens software (Scientific Volume Imaging) was used for deconvolution. The computational model of the mitochondrial network was made using Imaris 8 Bitplane AG, Zurich, Switzerland. The background of the raw fluorescence images was first corrected using the same algorithm in Huygens Essential® software (Scientific Volume Imaging, Hilversum, The Netherlands), which resulted in intensity-coded images of the mitochondrial network. Imaris 8.0® software was used for 3D processing and morphometric analysis. The colors define mitochondrial connectivity, with purple referring to fragmented mitochondria and red to extremely connected mitochondria.

### Glucose starvation analysis using IncuCyte ZOOM

To assess cell viability in response to glucose starvation, we used the IncuCyte ZOOM system in which the cell density and shape were observed by photonic microscopy while cells were maintained under standard culture conditions. HeLa cells were seeded at the density of 50,000 cells/well in a 24-well plate in regular medium (DMEM, 4.5 g/l glucose, 10% FBS, 1 mM sodium pyruvate and 1 mM glutamine). After 24 h, the medium was removed and cells were incubated in DMEM without glucose supplemented with 10% FBS, 1 mM sodium pyruvate and 1 mM glutamine. Real-time live-cell images were taken every 2 hours using IncuCyte ZOOM. For analysis of cell viability, well confluence (%) was automatically calculated during 84 h by using the Basic Analyzer segmentation mask of the IncuCyte ZOOM software 2015A. Despite the two filters used, cell area and eccentricity, the mask still recognized dead cells, which explains why the density for KO cells remains close to 100% at the end of the experiment.

### Electron microscopy

HeLa cells were seeded at the density of 500,000 cells/well in a six-well plate for 24 h and fixed in 4% formaldehyde, 2% glutaraldehyde and 0.1 M cacodylate (pH 7.4) for 2 h at room temperature then post-fixed in 1% osmium tetroxide for 1 h and stained in 0.5% uranyl acetate for another hour. The samples were then dehydrated in a graded series of 35%, 50%, 70%, 100% ethanol and exchanged to propylene oxide. After infiltration at 1:1 propylene oxide and epoxy resin (Poly/Bed 812, Polysciences, Warrington, PA) overnight, samples were embedded in 100% epoxy resin. Polymerization of resin was performed for 3 days at 55°C. Thin sections of 70–90 nm were cut with an ultramicrotome (Leica EM UC6, Leica Microsystems, Buffalo Grove, IL), stained with uranyl acetate and lead citrate, lightly carbon coated, and imaged in a Hitachi 7650 or 7600 transmission electron microscope (Hitachi High Technologies America, Gaithersburg, MD). Images were taken with a 2k×2k AMT digital camera (Advanced Microscopy Techniques, Woburn, MA).

### Western blotting

HeLa cells were cultured for 24 h in 25 cm<sup>2</sup> flasks. Protein lysates were prepared using RIPA buffer supplemented with 1× protease inhibitor cocktail (Roche), subjected to SDS-PAGE and transferred onto PVDF membranes (Amersham Hybond 0.45  $\mu$ m PVDF). The membranes were blocked for 1 h with 5% milk in Tris-buffered saline with 0.1% Tween 20 (TBST), then were incubated overnight with the following primary antibodies at 1:5000 dilution: rabbit polyclonal eIF3X (CLUH) antibody (Novus Biologicals, NB100-93306), total OXPHOS Human WB antibody cocktail (Abcam, ab110411), mouse monoclonal  $\alpha$ -tubulin antibody (Sigma Aldrich, T9026) and anti-VDAC1 antibody (Abcam, ab14734). The antibodies used for mitochondrial translation machinery (dilution of

1:5000) were against ERAL1 (Proteintech 11478-1-AP), MRPL44 (genetex GTX121263), MRPL13 (Proteintech 16241-1-AP), TUFM (Abnova H00007284-B01P), EFG1 (abcam ab204338), MRPS27 (Proteintech 17280-1-AP) and MRPS17 (Proteintech 18881-1-AP).

After washing in TBST, the membranes were incubated with horseradish peroxidase (HRP)-conjugated goat anti-mouse-IgG or anti-rabbit-IgG (1:10000 dilution) (GE Healthcare) for 1 h and then washed with TBST. Bands on immunoblots were detected by using SuperSignal West Femto Maximum Sensitivity Substrate (11859290, Pierce).

### Mitochondrial extraction and BN-PAGE

HeLa cells were cultured in 75 cm<sup>2</sup> flasks. 10<sup>7</sup> cells were harvested and suspended in 100  $\mu$ l PBS. 100  $\mu$ l of 4 mg/ml digitonine diluted in PBS was added, and cells were incubated for 10 min at 4°C under agitation. The mixture was washed twice with 1 ml PBS and mitochondria were harvested by centrifugation at 10,000 *g* for 10 min at 4°C. The mitochondrial pellet was suspended in AC/BT buffer (1.5 M amino-caproic acid and 75 mM bis-Tris, pH 7) for an approximate final protein concentration of 10 mg/ml. 25  $\mu$ g of mitochondrial proteins were suspended in AC/BT buffer for a final volume of 25  $\mu$ l, and 75  $\mu$ g laurylmaltoside was added to samples, which were then incubated under agitation for 10 min at 4°C. Samples were centrifuged at 20,000 *g* for 20 min at 4°C and supernatants were submitted to BN-PAGE in 3–12% gels. The proteins were then transferred onto PVDF membrane. The membrane was blocked for 1 h with 5% milk in TBST. Then, the membrane was blotted with the following antibodies at 1:1000 dilution: anti-NDUFS2 antibody (Abcam, ab110249), anti-UQCRC2 antibody (Abcam, ab14745), anti-MTCO1 antibody (Abcam, ab14705), anti-SDHA antibody (Abcam, ab14715) and anti-OXPHOS complex V subunit (Invitrogen, 12005645). The quantification of the different respiratory complexes was performed with Image J.

### Mitochondrial enzymatic activities

The activities of the mitochondrial OXPHOS complexes and citrate synthase (CS) were measured in WT and CLUH-KO mitochondrial-enriched fractions at 37°C with a UVmc2 spectrophotometer (SAFAS, Monaco). Activities of the succinate ubiquinone reductase (complex II), ubiquinol cytochrome *c* reductase (complex III), cytochrome *c* oxidase (complex IV) and citrate synthase (CS) were measured according to standard methods (Medja et al., 2009). Complex I activity was measured as described by Desquiret-Dumas et al. (2013) and F<sub>0</sub>F<sub>1</sub>-ATPase activity (complex V) was determined according to Rustin et al. (1994).

### Quantification of mtDNA copy number

For mtDNA quantification, total DNA was isolated from WT and CLUH KO HeLa cells by using a DNeasy Blood and tissues kit (Qiagen). qRT-PCRs were performed in triplicate in 96-well reaction plates (Applied Biosystems). Each reaction (final volume 10  $\mu$ l) contained 25 ng DNA, 5  $\mu$ l of Power SYBR-Green PCR Master Mix (Applied Biosystems) and 0.5  $\mu$ M of each forward and reverse primer. ND1, mitochondrial encoded gene, was amplified and  $\beta$ 2 microglobulin ( $\beta$ 2 m), nuclear encoded gene, was used as a normalizing control. Primers were: ND1-F, 5'-AAGTCACCCCTAGCCATC ATTCTAC-3' and ND1-R, GCAGGAGTAATCAGAGGTGTTCTT-3'; and  $\beta$ 2m-F, 5'-TGCTGTCTCCATGTTGATGTATCT-3' and  $\beta$ 2m-R, 5'-TCTCTGCTCCCCACCTCTAAGT-3'.

### mtDNA recovery after ethidium bromide-mediated depletion

WT and CLUH KO HeLa cells were seeded in six-well plates at 20% confluence. After 24 h, cells were incubated with or without 0.1  $\mu$ g/ml ethidium bromide. After 3 days, cells were washed three times with 2 ml of medium without ethidium bromide. After washing, cells were incubated in medium without ethidium bromide and mtDNA was quantified as described below after 2, 4, 6 and 8 days of recovery.

### mtDNA damage

mtDNA damage was quantified by long-range PCR to assess mtDNA deletions. One very long fragment PCR, covering the whole mtDNA genome and two long fragments PCR, designed to cover the whole mtDNA genome, were amplified. PCR products were analyzed by agarose gel electrophoresis



on 0.8% gels. Primer set 1 (forward ND5 to reverse COX1; forward, 5'-TACGTTGTAGCCCACTTCCACT-3' and reverse, 5'-GCCCCATGTG TAGGAAGAG-3') and primer set 3 (forward COX1 and reverse ND5; forward, 5'-AACTTCGGCTCACTCCTTGG-3' and reverse, 5'-AGTAA CGTCGGGGCATTCG-3'). Primer set 2 (forward, 5'-GGCACCCCTC TGACATCC-3' and reverse, 5'-TAGGTTTGAGGGGAATGCT-3') covers the whole mtDNA on one very long PCR product.

### ECAR measurement by using a Seahorse machine

WT and CLUH-KO cells were plated on an XF96 plate (Seahorse Biosciences) at 5000 and 20,000 cells/well and incubated for 24 h. ECAR was measured by using the XF96 Extracellular Flux Analyser according to the suggested protocols provided by Seahorse Bioscience.

### Krebs cycle analysis

Oxygraphic analyses were performed at 37°C on a high-resolution oxygraph (Oroboros, Innsbruck, Austria) as described previously (Desquiret-Dumas et al., 2013). Briefly, cells were permeabilized using digitonin at 20 µg for 10<sup>6</sup> cells, then after washing in respiratory buffer, 3×10<sup>6</sup> permeabilized cells were placed in 2 ml respiratory buffer in an oxygraphic chamber. Respiration rates were measured on cells after adding substrates or inhibitors.

### Measurement of pyruvate consumption and citrate production:

Pyruvate (2.5 mM) and malate (5 mM) were added in the oxygraphic chamber, and a 1 ml aliquot was immediately removed for acid organic analysis. At 5 min after substrate additions, a sub-saturating ADP concentration (0.5 mM) was added, which allowed a stimulation of phosphorylating respiration at nearly 50% of the maximal mitochondrial respiratory rate ( $V_{\max}$ ) in control cells. Precisely 30 min after ADP addition, a new 1 ml aliquot was taken from the oxygraphic chambers for the acid organic analysis. Oxygen consumption was controlled during all the experiment. For both aliquots, 200 µl of 7% perchloric acid was added to quench the reactions. After 10 s of stirring, the aliquots were immediately frozen in liquid nitrogen and thawed at 37°C to lyse mitochondria. Then, tubes were centrifuged for at 20,000 g for 5 min at 4°C. The pellet was used for protein concentration and the supernatant was conserved at −80°C until analysis. The metabolites were extracted by ethyl acetate, evaporated, silylated and injected in a gas chromatography (GC) mass spectrophotometer (GCMS-2010C, Shimadzu). Peaks were identified and quantified using GC solution software (Shimadzu) with an existing library.

### Measurement of respiration after adding Krebs cycle substrates

Respirations rates were measured on permeabilized cells after adding sequentially: (1) 2.5 mM pyruvate and 5 mM malate (M+P); (2) 5 mM isocitrate (M+P+I); (3) 5 mM glutamate (M+P+I+G); (4) 5 mM  $\alpha$ -ketoglutarate (M+P+I+G+KG); (5) 10 mM succinate (M+P+I+G+KG+S); and (6) 5 µM rotenone (M+P+I+G+KG+S+R) to inhibit complex I activity and thus determining the maximal complex II-linked respiration. All the respiration rate measurements were conducted at saturating ADP concentration (1 mM ADP) to induce the maximal phosphorylating respiration.

$\beta$ -oxidation was investigated by following the respirations rates in 6×10<sup>6</sup> permeabilized cells after supplying 1 mM carnitine, 5 mM malate and 100 µM palmytoyl-CoA.

### Mitochondrial protein synthesis

The labeling of newly translated mitochondrial proteins was performed as described previously (Chomyn, 1996). Briefly, cells were seeded in six-well plates and treated with 100 µg/ml emetine for 20 min to inhibit cytosolic protein synthesis. [<sup>35</sup>S]methionine was then added to the cells and incubated for 45 min. Cells were then collected and lysed, and 25 µg proteins were separated by SDS-PAGE. Gels were stained with Coomassie Blue, dried and exposed to phosphor plates for 72 h. The <sup>35</sup>S signal was read by using a TyphoonTM Phosphorimager (GE Healthcare).

### Metabolite extraction

WT and CLUH-KO HeLa cells were cultured in ten different 75 cm<sup>2</sup> flasks. When 70% confluence was obtained, the culture medium was removed and

cells were harvested by trypsinization and washed twice in a cold 1× PBS solution with 10% fetal bovine serum (ThermoFisher). After centrifugation (300 g for 5 min at 4°C), the supernatant was eliminated and the cell pellet was dissolved in 100 µl of a cold 1× PBS solution. 50 µl was used for determining protein dosage, and the remaining 50 µl (~2×10<sup>6</sup> cells) was used for the extraction of metabolites. The metabolic quenching was completed by adding 100 µl of a cold ethanol and 1× PBS mixture (85:15, v/v) to the cell pellet obtained after a second run of centrifugation (300 g for 5 min at 4°C) and elimination of the supernatant. After vortexing, the mixture was transferred to a 0.5 ml homogenizer tube prefilled with ceramic beads. Cell lysis and protein extraction was achieved in a Precellys®24 homogenizer (Bertin Corp., Rockville, MD) by two cycles of grinding (40 s at 6500 rpm, followed by 30 s at 6000 rpm) at 4°C. The resulting homogenate was centrifuged at 20,000 g for 10 min at 4°C and the supernatant was stored at −80°C until analysis. We applied a targeted, quantitative metabolomic approach to the cell extracts using the Biocrates AbsoluteIDQ p180 kit (Biocrates Life sciences AG, Innsbruck, Austria). This kit, in combination with a AB Sciex QTRAP 5500 (Life Sciences SCIEX, Villebon sur Yvette, France) mass spectrometer, enables quantification of up to 188 different endogenous molecules, including acylcarnitines, amino acids, biogenic amines, glycerophospholipids, sphingolipids and sugar. Samples were prepared according to the Biocrates Kit user manual. After validation of the three levels of quality controls (QCs) used in the kit, the metabolite concentrations were normalized with respect to protein cell extract concentrations.

### Metabolomics data analysis

Orthogonal partial least squares discriminant analysis (OPLS-DA), a supervised method of pattern recognition, was further used to maximize the variations between groups and to determine the contributing variables. The quality of models was validated by determining two parameters: R<sup>2</sup> (goodness of fit) and Q<sup>2</sup> cumulated (goodness of prediction). In the model with the best predictive capabilities, variables were selected on the basis of the variable importance in the projection (VIP) and loading values. VIP values summarize the importance of each variable for the OPLS-DA model, whereas loading values summarize the importance of each X variable in approaching the variance of X captured by the latent variable. Variables with a VIP value greater than 1 are considered important for group discrimination in predictive models. Plotting VIP versus loading values – to make a so-called ‘volcano’ plot – allows the selection of important variables in PLS models. Multivariate data analysis was conducted by using the SIMCA-P software 13.0 (Umetrics, Umeå, Sweden).

### Acknowledgements

We are grateful to all the MitoLab colleagues, especially Drs Savennières and Layon, for their permanent support, inspiration, constructive discussions and critical reading of the manuscript.

### Competing interests

The authors declare no competing or financial interests.

### Author contributions

Conceptualization: J.W., D.G., D.C.L., G.L., S.K.; Methodology: J.W., D.G., R.P., N.G., V.D.-D., J.M.C.d.I.B., I.D.R., F.M., M.L.M., S.C., A.C.; Validation: J.W., D.G., R.P., N.G., V.D.-D., I.D.R., F.M., M.L.M., S.C., A.C.; Formal analysis: J.W., J.M.C.d.I.B., I.D.R., V.P., D.B., D.C.L., P.R., G.L., S.K.; Investigation: J.W., D.G., R.P., N.G., V.D.-D., J.M.C.d.I.B., I.D.R., F.M., M.L.M., S.C., A.C.; Resources: J.W., D.B., D.C.L., P.R., G.L., S.K.; Supervision: D.C.L., P.R., G.L., S.K. The corresponding authors are G.L. and S.K.

### Funding

We acknowledge support from the Institut National de la Santé et de la Recherche Médicale (INSERM), Centre National de la Recherche Scientifique (CNRS), the Université Angers, the University Hospital of Angers, the Région Pays de Loire and Angers Loire Métropole. This work was also supported by grants from the following patients' foundations: 'Fondation VISIO', 'Ouvrir les Yeux', 'Union Nationale des Aveugles et Déficiants Visuels', 'Association contre les Maladies Mitochondriales', 'Retina France' and 'Kjer France'.

## Supplementary information

Supplementary information available online at  
<http://jcs.biologists.org/lookup/doi/10.1242/jcs.201616.supplemental>

## References

- Benard, G. and Rossignol, R.** (2008). Ultrastructure of the mitochondrion and its bearing on function and bioenergetics. *Antioxid Redox Signal*, **10**, 1313–1342.
- Benard, G., Faustin, B., Passerieux, E., Galinier, A., Rocher, C., Bellance, N., Delage, J.-P., Casteilla, L., Letellier, T. and Rossignol, R.** (2006). Physiological diversity of mitochondrial oxidative phosphorylation. *Am. J. Physiol. Cell Physiol.* **291**, C1172–C1182.
- Chomyn, A.** (1996). In vivo labeling and analysis of human mitochondrial translation products. *Methods Enzymol.* **264**, 197–211.
- Cox, R. T. and Spradling, A. C.** (2009). Clueless, a conserved Drosophila gene required for mitochondrial subcellular localization, interacts genetically with parkin. *Dis. Model Mech.* **2**, 490–499.
- Davies, K. M., Anselmi, C., Wittig, I., Faraldo-Gomez, J. D. and Kuhlbrandt, W.** (2012). Structure of the yeast F1Fo-ATP synthase dimer and its role in shaping the mitochondrial cristae. *Proc. Natl. Acad. Sci. USA* **109**, 13602–13607.
- Desquret-Dumas, V., Gueguen, N., Leman, G., Baron, S., Nivet-Antoine, V., Chupin, S., Chevrollier, A., Vessieres, E., Ayer, A., Ferre, M. et al.** (2013). Resveratrol induces a mitochondrial complex I-dependent increase in NADH oxidation responsible for sirtuin activation in liver cells. *J. Biol. Chem.* **288**, 36662–36675.
- El Zawily, A. M., Schwarlander, M., Finkemeier, I., Johnston, I. G., Benamar, A., Cao, Y., Gissot, C., Meyer, A. J., Wilson, K., Datla, R. et al.** (2014). FRIENDLY regulates mitochondrial distribution, fusion, and quality control in Arabidopsis. *Plant Physiol.* **166**, 808–828.
- Fields, S. D., Conrad, M. N. and Clarke, M.** (1998). The *S. cerevisiae* CLU1 and *D. discoideum* cluA genes are functional homologues that influence mitochondrial morphology and distribution. *J. Cell Sci.* **111**, 1717–1727.
- Fields, S. D., Arana, Q., Heuser, J. and Clarke, M.** (2002). Mitochondrial membrane dynamics are altered in cluA- mutants of Dictyostelium. *J. Muscle Res. Cell Motil.* **23**, 829–838.
- Gao, J., Schatton, D., Martinelli, P., Hansen, H., Pla-Martin, D., Barth, E., Becker, C., Altmueller, J., Frommolt, P., Sardiello, M. et al.** (2014). CLUH regulates mitochondrial biogenesis by binding mRNAs of nuclear-encoded mitochondrial proteins. *J. Cell Biol.* **207**, 213–223.
- Gehrke, S., Wu, Z., Klinkenberg, M., Sun, Y., Auburger, G., Guo, S. and Lu, B.** (2015). PINK1 and Parkin control localized translation of respiratory chain component mRNAs on mitochondria outer membrane. *Cell Metab.* **21**, 95–108.
- Haga, N., Fujita, N. and Tsuruo, T.** (2003). Mitochondrial aggregation precedes cytochrome c release from mitochondria during apoptosis. *Oncogene* **22**, 5579–5585.
- Kohen, R., Yamamoto, Y., Cundy, K. C. and Ames, B. N.** (1988). Antioxidant activity of carnosine, homocarnosine, and anserine present in muscle and brain. *Proc. Natl. Acad. Sci. USA* **85**, 3175–3179.
- Langer, W., Sohler, F., Leder, G., Beckmann, G., Seidel, H., Grone, J., Hummel, M. and Sommer, A.** (2010). Exon array analysis using re-defined probe sets results in reliable identification of alternatively spliced genes in non-small cell lung cancer. *BMC Genomics* **11**, 676.
- Lee, J.-Y., Nagano, Y., Taylor, J. P., Lim, K. L. and Yao, T.-P.** (2010). Disease-causing mutations in parkin impair mitochondrial ubiquitination, aggregation, and HDAC6-dependent mitophagy. *J. Cell Biol.* **189**, 671–679.
- Lee, J., Ellis, J. M. and Wolfgang, M. J.** (2015). Adipose fatty acid oxidation is required for thermogenesis and potentiates oxidative stress-induced inflammation. *Cell Rep.* **10**, 266–279.
- Liu, H., D'Andrade, P., Fulmer-Smentek, S., Lorenzi, P., Kohn, K. W., Weinstein, J. N., Pommier, Y. and Reinhold, W. C.** (2010). mRNA and microRNA expression profiles of the NCI-60 integrated with drug activities. *Mol. Cancer Ther.* **9**, 1080–1091.
- Logan, D. C., Scott, I. and Tobin, A. K.** (2003). The genetic control of plant mitochondrial morphology and dynamics. *Plant J. Cell Mol. Biol.* **36**, 500–509.
- Medja, F., Allouche, S., Frachon, P., Jardel, C., Malgat, M., de Camaret, B. M., Slama, A., Lunardi, J., Mazat, J. P. and Lombès, A.** (2009). Development and implementation of standardized respiratory chain spectrophotometric assays for clinical diagnosis. *Mitochondrion* **9**, 331–339.
- Mi, H., Muruganujan, A., Casagrande, J. T. and Thomas, P. D.** (2013). Large-scale gene function analysis with the PANTHER classification system. *Nat. Protoc.* **8**, 1551–1566.
- Mukhopadhyay, P., Rajesh, M., Haskó, G., Hawkins, B. J., Madesh, M. and Pacher, P.** (2007). Simultaneous detection of apoptosis and mitochondrial superoxide production in live cells by flow cytometry and confocal microscopy. *Nat. Protoc.* **2**, 2295–2301.
- Nguyen, T. T., Oh, S. S., Weaver, D., Lewandowska, A., Maxfield, D., Schuler, M.-H., Smith, N. K., Macfarlane, J., Saunders, G., Palmer, C. A. et al.** (2014). Loss of Miro1-directed mitochondrial movement results in a novel murine model for neuron disease. *Proc. Natl. Acad. Sci. USA* **111**:E3631–E3640.
- Nishimura, K., Nakatsu, F., Kashiwagi, K., Ohno, H., Saito, T. and Igarashi, K.** (2002). Essential role of S-adenosylmethionine decarboxylase in mouse embryonic development. *Genes Cells* **7**, 41–47.
- Pendeville, H., Carpino, N., Marine, J.-C., Takahashi, Y., Muller, M., Martial, J. A. and Cleveland, J. L.** (2001). The ornithine decarboxylase gene is essential for cell survival during early murine development. *Mol. Cell Biol.* **21**, 6549–6558.
- Reinhold, W. C., Sunshine, M., Liu, H., Varma, S., Kohn, K. W., Morris, J., Doroshow, J. and Pommier, Y.** (2012). CellMiner: a web-based suite of genomic and pharmacologic tools to explore transcript and drug patterns in the NCI-60 cell line set. *Cancer Res.* **72**, 3499–3511.
- Rustin, P., Chretien, D., Bourgeron, T., Gérard, B., Rötig, A., Saudubray, J. M. and Munnich, A.** (1994). Biochemical and molecular investigations in respiratory chain deficiencies. *Clin. Chim. Acta* **228**, 35–51.
- Schatton, D., Pla-Martin, D., Marx, M.-C., Hansen, H., Mourier, A., Nemazanyy, I., Pessia, A., Zentis, P., Corona, T., Kondylis, V. et al.** (2017). CLUH regulates mitochondrial metabolism by controlling translation and decay of target mRNAs. *J. Cell Biol.* **216**, 675–693.
- Sen, A. and Cox, R. T.** (2016). Clueless is a conserved ribonucleoprotein that binds the ribosome at the mitochondrial outer membrane. *Biology Open* **5**, 195–203.
- Sen, A., Kalvakuri, S., Bodmer, R. and Cox, R. T.** (2015). Clueless, a protein required for mitochondrial function, interacts with the PINK1-Parkin complex in Drosophila. *Dis. Model Mech.* **8**, 577–589.
- Wang, Z. H., Clark, C. and Geisbrecht, E. R.** (2016). Drosophila clueless is involved in Parkin-dependent mitophagy by promoting VCP-mediated Marf degradation. *Hum. Mol. Genet.* **25**, 1946–1964.
- Zhu, Q., Hulen, D., Liu, T. and Clarke, M.** (1997). The cluA- mutant of Dictyostelium identifies a novel class of proteins required for dispersion of mitochondria. *Proc. Natl. Acad. Sci. USA* **94**, 7308–7313.
- Zick, M., Rabl, R. and Reichert, A. S.** (2009). Cristae formation-linking ultrastructure and function of mitochondria. *Biochim. Biophys. Acta* **1793**, 5–19.